www.springer.com/41230
https://doi.org/10.1007/s41230-025-5108-8
Research & Development
Vol. 23 No. 4 July 2026
CHINA FOUNDRY

Interfacial microstructure and properties of additively manufactured composite rollers after online service

Xin Di[1, 2], Hao-zheng Li[1, 2], *Ce Ji[1, 2], Peng-rui Li[3, 4], Shi-bin Liu[5], Jin-feng Chen[6], Wei-guo Han[5], and **Hua-gui Huang[1, 2]

1. College of Mechanical Engineering, Yanshan University, Qinhuangdao 066004, Hebei, China
2. National Engineering Research Center for Equipment and Technology of Cold Strip Rolling, Yanshan University, Qinhuangdao 066004, Hebei, China
3. Changbai Mechanical & Electrical Equipment Maintenance Co., Ltd., Tangshan Caofeidian Industrial Zone, Tangshan 063200, Hebei, China
4. Hebei Metallurgical Continuous Casting Equipment Remanufacturing Technology Innovation Center, Tangshan 063200, Hebei, China
5. State Key Laboratory of High Performance Roll Materials and Composite Forming, Sinosteel Xingtai Machinery & Mill Roll Co., Ltd., Xingtai 054000, Hebei, China
6. Technology Center, Taiyuan Heavy Industry Co., Ltd., Taiyuan 030024, China

Abstract: Composite rollers serve as critical components in modern slab continuous casting systems, particularly the No. 0 segment rollers positioned at the mold exit, which endure severe service conditions and intermittent thermal shocks. The service stability of these composite rollers directly determines the continuous operation capability of casting lines and per-ton steel cost control, making reliability enhancement a critical research topic in the field of metallurgical equipment. In this study, 414N/42CrMo heterogeneous composite rollers with gradient properties were fabricated by additive manufacturing. The multi-scale characterization techniques were conducted on the composite rollers after online service for 2.5 months in a continuous casting line, including SEM, EBSD, and X-ray computed tomography for 3D defect mapping. The elemental interdiffusion kinetics, microstructure, and defect distribution were systematically elucidated. The directional migration of Cr/Mo elements enables the formation of a gradient interfacial architecture: heterogeneous interfacial thickness with alternating peak-valley morphology driven by differential elemental diffusion behaviors, progressive transitions in grain boundary configurations from low-angle to high-angle, and gradient variations in grain size distribution across adjacent microstructural zones. X-ray computed tomography reveals that the defect distribution across the entire interfacial region exhibits spatial heterogeneity, characterized by the presence of distinct defect clusters from the 414N cladding layer near the interface, accompanied by localized aggregations of irregular defects (with an equivalent diameter greater than 50 μm). Therefore, a remanufacturing strategy is proposed to eliminate defect-rich interfacial layers and reconstruct gradient-compatible interfaces for performance restoration, which offers practical solutions for extending service life through precision remanufacturing.

Keywords: composite rollers; gradient material; microstructure; microscale defects; additive manufacturing

CLC numbers: TG142.33 **Document code:** A **Article ID:** 1672-6421(2026)04-577-14

***Ce Ji**

Ph. D., Associate Professor and Doctoral Supervisor. His research interests mainly focus on heterogeneous metal forming technology and equipment. He has led more than 10 projects funded by the National Science Foundation of China, the Science and Technology Program of Hebei, among others. To date, he has published over 40 journal articles and holds over 30 invention patents.

E-mail: jice@ysu.edu.cn

****Hua-gui Huang**

E-mail: hhg@ysu.edu.cn
Received: 2025-05-12; Revised: 2025-06-26; Accepted: 2025-08-20

1 Introduction

How to extend the service life of composite roller, a key load-bearing part in steel continuous casting lines, has become the bottleneck of modern efficient continuous casting production due to factors like thermo-mechanical coupled loads, high-temperature oxidation corrosion, and solid-state phase transformations[1, 2]. Thus, developing efficient remanufacturing technologies to enhance service performance and reuse the waste rollers has become a crucial way to reduce production costs[3]. In recent years, additive manufacturing (AM) technology, with near-net shaping advantage, gradient material design capability, and digital manufacturing characteristics, has offered an innovative solution for high-performance remanufacturing[4,5]. Especially in the remanufacturing of continuous casting composite rollers, the application of AM technology provides a new way to significantly improve their properties and service life[6-8].

As a core component of the slab continuous casting production line, the wear resistance and service life of the composite rollers directly determine the work efficiency and production costs of the entire factory[9,10]. During the slab continuous casting process, the No. 0 segment rollers endure complex loading conditions, primarily categorized into mechanical loads and cyclic thermal loads[11]. Under the high-temperature, high-pressure, and high-wear conditions of continuous casting environments, the thermal-mechanical wear failure of AM rollers, which constrains the performance and service life, remains a persistent research focus[12,13]. Consequently, periodic inspection of defects or damage and timely repair of composite rollers are imperative[14]. Current repair methods for composite rollers primarily include wire arc additive manufacturing (WAAM), laser cladding technology, and composite casting technology. For example, the WAAM achieves the geometric reconstruction of damaged areas through layer-by-layer deposition[15-17]. Laser cladding technology enables precise metallurgical bonding via high-energy beam irradiation[18-20]. Composite casting technology realizes interfacial metallurgical restoration through secondary casting processes[21-23]. These techniques enable the precise formation of desired coatings on component surfaces, serving both to restore the performance of damaged parts through repair and to provide additional protection or functional coatings during the manufacturing of new components[24-25].

The emergence of WAAM has revolutionized the fabrication of complex metallic components, but the layer-by-layer deposition process inherently introduces non-equilibrium metallurgical characteristics, leading to significant gradients in composition, microstructure, and mechanical properties along the wall thickness direction from the surface to the substrate interface[26-28]. These gradients arise from rapid solidification kinetics, thermal cycling, and heterogeneous interface fusion, which are especially pronounced in components with intricate wall geometries[29]. Furthermore, the interface often suffers from poor bonding strength due to factors like cracks and intermetallic compounds. Therefore, enhancing the quality of metallurgical bonding can significantly improve the service life. For instance, Liu et al.[30] successfully fabricated a defect-free metallurgical bonding interface between aluminum bronze and steel by optimizing the interfacial melting process. This interface demonstrated a 13.3% increase in yield strength (119.6 MPa), a 39% increase in ultimate tensile strength (558.7 MPa), and an 83.9% increase in elongation (51.5%). Therefore, it can be inferred that the metallurgical bonding interface contributes to effectively mitigating interfacial stress concentration and suppressing crack propagation, thereby enhancing the structural integrity of the entire component.

In order to achieve a strong metallurgical bonding at heterogeneous interfaces, constructing a gradient composite interface to address the significant performance differences between heterogeneous materials has become an effective technical approach. In functionally graded AM, distinct zones exhibit unique gradient behaviors[31]. For the interface bonding zone, limited interdiffusion between dissimilar materials or layers can lead to brittle intermetallic compounds or micro-defects, posing challenges to structural integrity[32]. For now, it has been proven that gradient design can effectively suppress the formation of brittle intermetallic compounds while achieving synergistic enhancement of strength and toughness through dislocation density gradients and bimodal grain size distribution[33,34]. However, existing studies have predominantly focused on static performance evaluations of laboratory-repaired small samples, with significant deficiencies remaining in research on full-size continuous casting rollers after actual online service conditions. For the surface and core of continuous casting composite rollers, the dynamic thermomechanical coupling effects induced by cyclic temperature fluctuations during service will lead to coordinated evolution of residual stress redistribution, elemental diffusion, and micro-defects within the gradient layer. Ultimately, performance degradation would occur along the wall-thickness direction[35,36]. Currently, conventional offline physical simulation, such as isothermal-mode high-temperature tribological testing, proves inadequate for simulating multi-field coupled damage behavior under actual operating conditions. Therefore, due to production costs, the WAAM is currently the most optimal choice for achieving industrial production. Besides, analyzing the performance of the composite rollers fabricated by the WAAM after online service becomes an important way to verify whether the product can meet the industrial requirements.

Therefore, the investigation specifically focused on revealing the microstructural characteristics of 414N/42CrMo composite rollers fabricated by the WAAM after online service. The characterization techniques, including optical microscopy (OM), scanning electron microscopy (SEM), electron backscatter diffraction (EBSD), and synchrotron radiation X-ray computed tomography, were employed to elucidate element interdiffusion behavior at heterogeneous interfaces and stress redistribution mechanisms. The results contribute to establishing theoretical foundations for the optimized design and intelligent remanufacturing of composite rollers with enhanced longevity.

2 Experimental methods

The experimental composite roller investigated in this study was the No. 0 segment roller used in a continuous casting machine and has serviced online for 2.5 months. Figure 1(a) schematically illustrates the manufacturing process of rollers based on the WAAM technology. After each service, the surface of the composite roller wears down and the size decreases. To restore to the original size, the surface fatigue layer needs to be removed by turning, and then the WAAM process was used to achieve remanufacturing. The 414N wires with a diameter of 1.2 mm were used to deposit gradient materials on the 42CrMo substrate. The technical procedure involved two sequential stages: A circumferential single-layer cladding deposition was initially performed along the substrate periphery to establish a dense metallurgical bonding layer. Subsequently, multi-layer multi-pass cladding deposition was conducted by a program-controlled coaxial gas-shielded arc welding system following predefined model trajectories. This layer-by-layer accumulation continued until the required dimensional specifications for roller restoration. Critical process parameters included a nozzle-to-substrate distance of 8–10 mm, a deposition speed of 8–15 mm·s^{-1}, and a high-purity argon shielding gas flow rate of 10 L·min^{-1} (purity≥99.99%) to protect the molten pool. Additionally, 42CrMo substrate preheating was implemented to eliminate cracks during deposition. The welding gun was perpendicular to the substrate deposition surface, the welding wire was tilted at an angle of 30°–45° relative to the welding gun, and the welding current was 130–160 A.

The elemental compositions of 42CrMo and 414N are shown in Table 1. The samples after online serviced for 2.5 months were extracted along the wall thickness direction, as shown in Figs. 1(b) and (c). For microstructural observation, the specimens were ground using abrasive papers with sequential grit sizes (360, 600, 1200, 2000, and 3000), followed by polishing with silica suspension to achieve a mirror finish. The microstructures of samples were observed by OM (Zeiss Axiovert 40 MAT), SEM (FEI Scios 2 DualBeam), and EBSD (Nordly Max 3). EBSD characterization using an accelerating voltage of 20 kV, working distance of 15 mm, an inclination of 70°, and step sizes of 1.5 μm (low-magnification) and 0.6 μm (high-magnification) was employed for multi-scale analysis. To eliminate the surface stress layer caused by mechanical polishing, the Leica EM RES102 ion beam milling system was used to thin the sample. The working current was 2.7 mA, and the voltage was 6.5 kV. The EBSD data were analyzed using an orientation imaging microscope (OIM) software.

Furthermore, to observe the defect distribution in the composite rollers after online service, samples were taken from the 414N and the bonding interface, as illustrated in view regions (1) and (2) in Fig. 1(c), where r is the radius and h is the height of the sample. Synchrotron radiation X-ray computed tomography was performed using a synchrotron radiation X-ray micro-computed tomography instrument, XLAB-2000, produced by Weikuang Technology (Suzhou) Co., Ltd., Suzhou, China. The instrument could achieve a voltage range of 40–160 kV, a maximum power of 25 W, and a spatial resolution of 0.5 μm. The experimental apparatus for X-ray micro-computed tomography tests and the process for 3D visualization are shown in Fig. 2. During the entire scanning stage, micro-CT was performed using a target current of 90 μA and an accelerating voltage of 80 kV, and the pixel resolution was 2 μm.

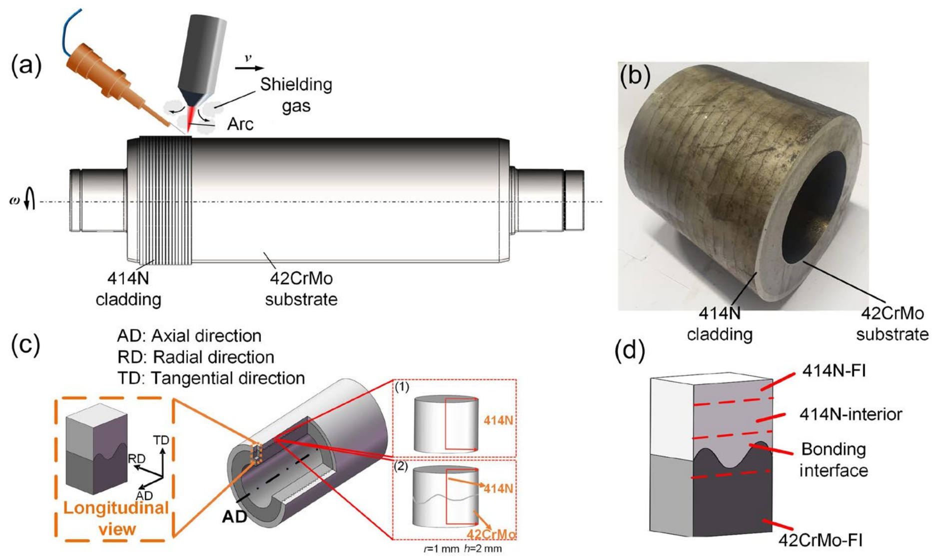

Fig. 1: Schematic diagram of additive manufacturing repair process for composite rollers (a), composite rollers after online service (b), microstructure sampling and tomography sampling (c), and schematic diagram of bonding interface partition (d)

Table 1: Compositions of 42CrMo and 414N materials (wt.%)

Element	C	Si	Mn	Cr	Ni	Mo	Fe
414N	≤0.08	0.55	1.30	13.35	4.00	0.7	Bal.
42CrMo	0.45	0.26	0.74	1.09	≤0.30	0.22	Bal.

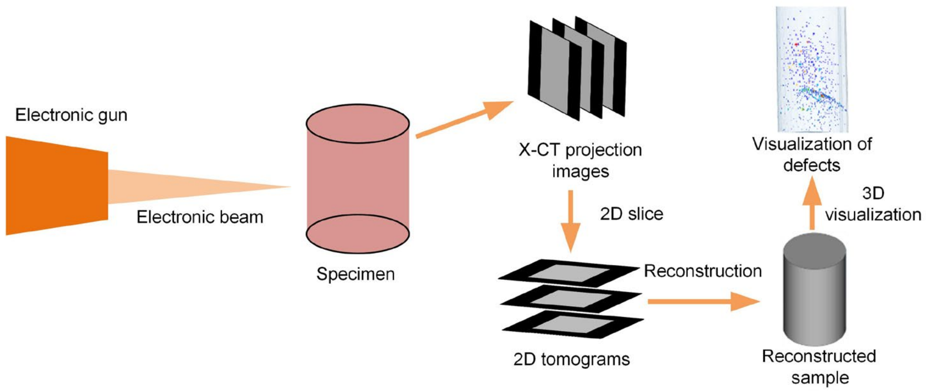

Fig. 2: Experimental apparatus and 3D visualization based on X-ray micro-computed tomography technology

3 Results and discussion

3.1 Metallic structures after online service

Figure 3 displays the metallographic structure of the composite rollers sampled via the method shown in Fig. 1(b). Region 414N-FI represents the far-interface zone and exhibits lath martensite structures, as shown in Fig. 3(a). In contrast, the 414N cladding interior region demonstrates equiaxed martensite morphology, as shown in Fig. 3(b). High-magnification OM observations reveal enhanced structural differentiation. The 414N-FI zone displays uneven grain size distribution compared to the 414N cladding interior region with predominantly equiaxed grains. The bonding interfacial zone presents complex phase configurations requiring multimodal characterization. Meanwhile, the 42CrMo substrate shows refined pearlite (P) and ferrite (F) microstructures. This functionally graded interface extending from the martensitic cladding to the ferritic-pearlitic substrate is formed due to the thermal gradients during both in-service continuous casting and repair deposition processes.

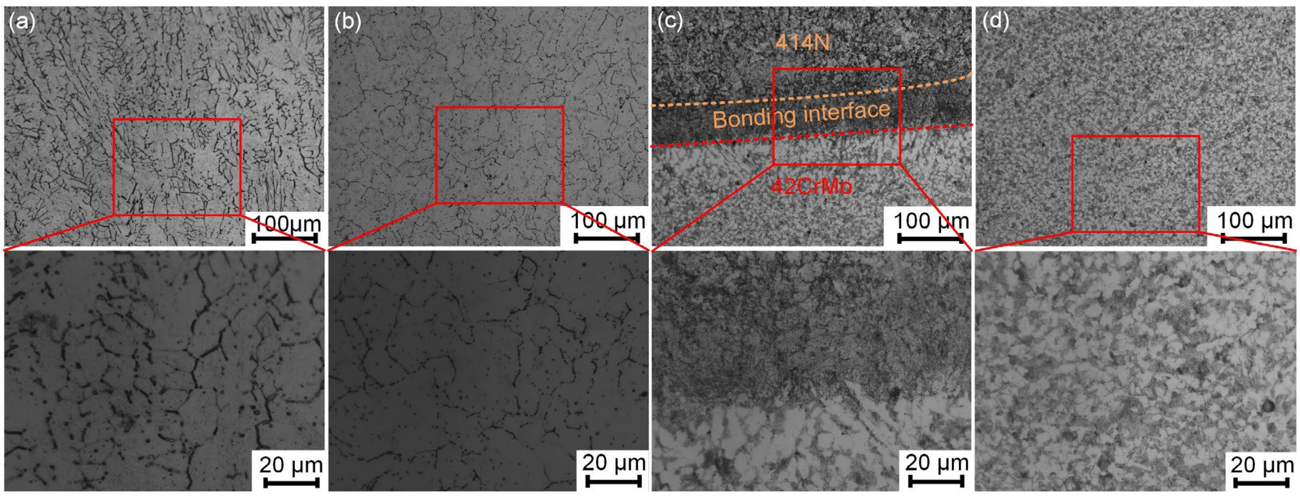

Fig. 3: Microstructure under different positions of composite rollers after online service: (a) 414N-FI; (b) 414N cladding interior; (c) bonding interface; (d) 42CrMo

3.2 Interfacial element distribution after online service

As shown in Fig. 4, the bonding interface exhibits distinct undulating morphological characteristics in SEM micrographs. Analytical results indicate that the temperature gradient effect within the molten pool induces intense thermal fluctuations at the interface, ultimately forming a periodic interfacial structure with alternating peak-valley features. Besides, EDS elemental mapping analyses reveal pronounced elemental concentration gradients across both the interfacial valleys in Fig. 5 and interfacial peaks in Fig. 6. The gradual color transition in Fig. 5 and Fig. 6 between different regions demonstrates significant interdiffusion of alloy elements (Fe, Cr, and Mn) at the interface, providing direct experimental evidence for the formation of interfacial diffusion layers.

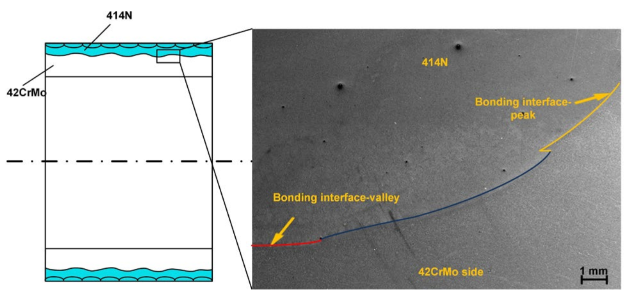

Fig. 4: Schematic diagrams and SEM images of peaks and valleys at bonding interface

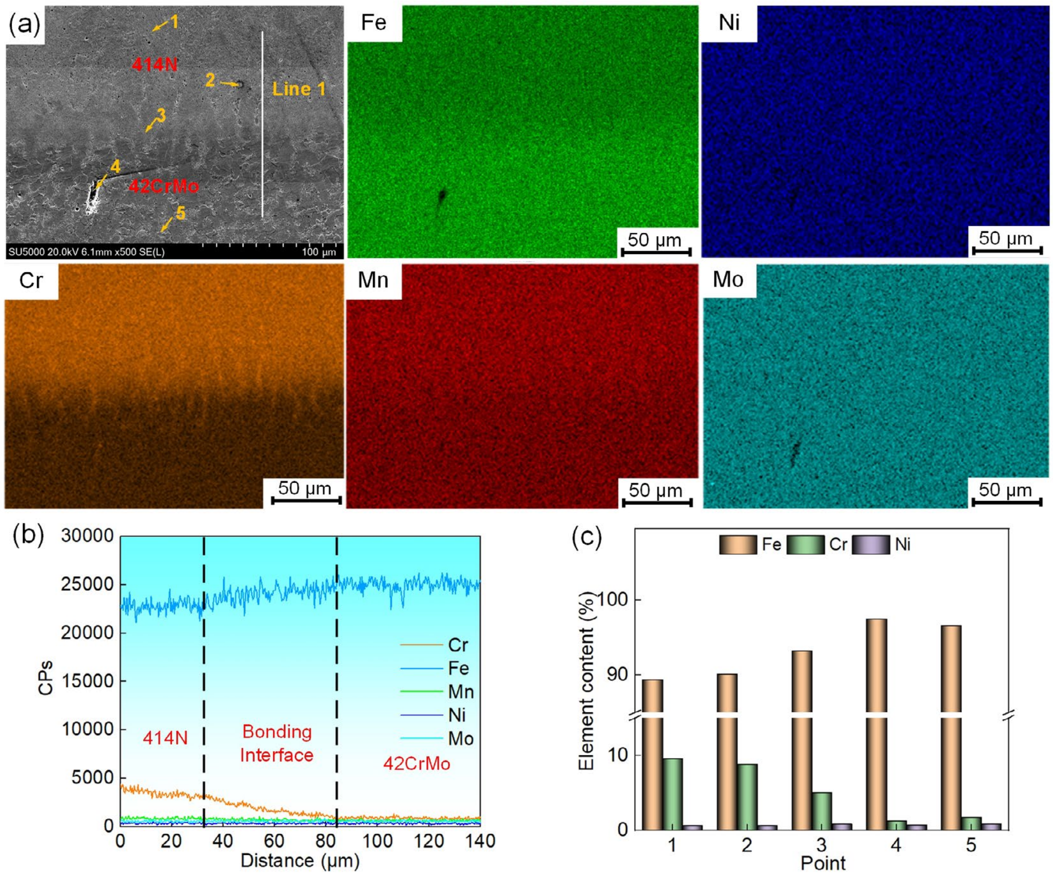

Fig. 5: SEM-EDS mapping results of valleys at 414N-42CrMo bonding interface: (a) elemental mapping; (b) line-scan; (c) point-scan

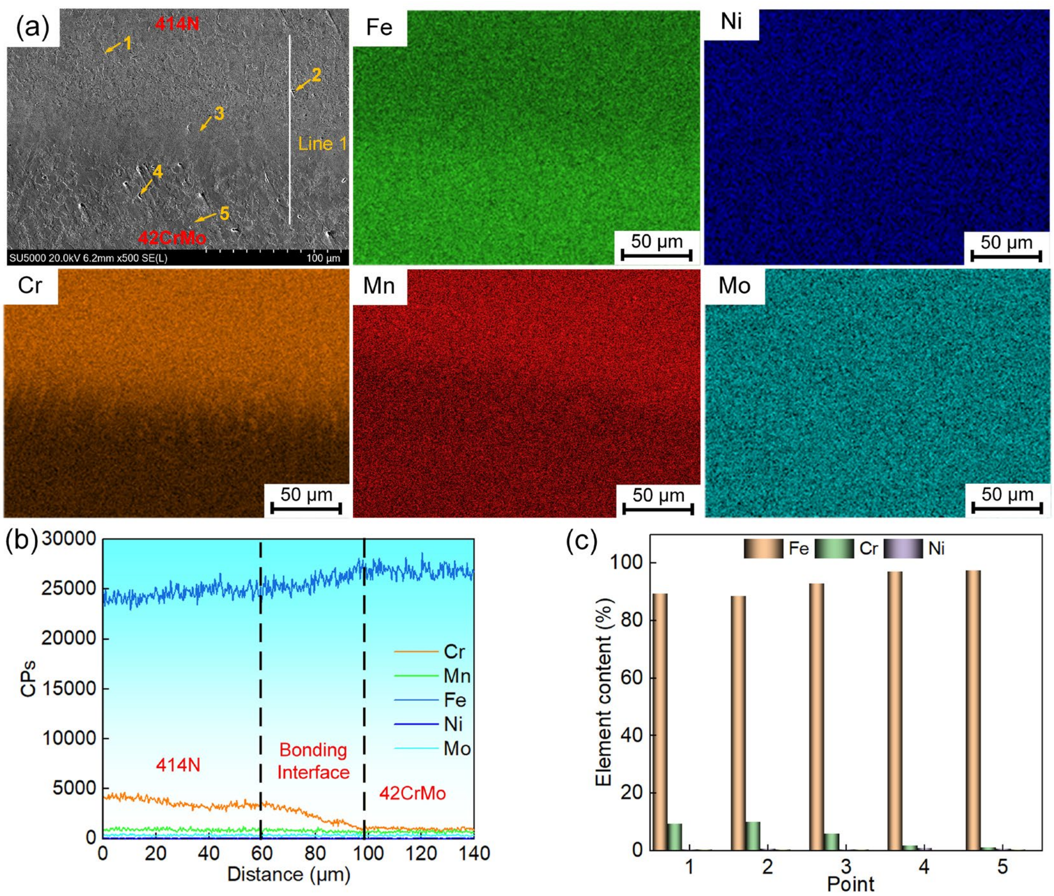

Fig. 6: SEM-EDS mapping results of peaks at 414N-42CrMo bonding interface: (a) elemental mapping; (b) line-scan; (c) point-scan

As evidenced by the linear scanning profiles in Figs. 5(b) and 6(b), the diffusion layer thickness demonstrates significant heterogeneity, measuring approximately 38 μm at the interfacial peak compared to 55 μm at the valley region. This dimensional discrepancy in diffusion layers is attributed to the non-uniform temperature distribution during the surfacing process. The elevated temperature at the molten pool center promotes enhanced elemental intermixing, resulting in a more extensive diffusion zone. Conversely, the relatively lower thermal energy at the molten pool side restricts atomic diffusion, leading to the formation of narrower transition zones. Notably, this thermally driven differential diffusion mechanism fundamentally contributes to the peak-valley morphology through periodic variations in elemental redistribution to achieve metallurgical bonding at the bonding interface[17].

3.3 Grain characteristics after online service

Figure 7 presents inverse pole figure (IPF) maps of four characteristic regions in the 414N-42CrMo system. The 414N-FI region is shown in Fig. 7(a), the 414N cladding interior region is displayed in Fig. 7(b), the bonding interface region is illustrated in Fig. 7(c), and the 42CrMo-FI region is depicted in Fig. 7(d). The corresponding grain size distribution histograms for these regions are presented in Fig. 8. The cladding boundary region exhibits a broad grain size distribution ranging from 5 to 60 μm with an average grain size of 16.5 μm, as shown in Fig. 8(a). The cladding interior region demonstrates a higher density of equiaxed grains, showing a narrower grain size distribution compared to the 414N-FI region, with an average size of 12.1 μm, as shown in Fig. 8(b). At the bonding interface region, the average grain size further decreases to 10.1 μm, as shown in Fig. 8(c), due to dynamic recrystallization induced by the 42CrMo substrate. Quantitative analysis reveals a distinct grain size gradient extending from the cladding layer to the substrate matrix.

To further quantify the gradient distribution characteristics, high-magnification EBSD tests were conducted. Figure 9 presents the IPF maps and Fig. 10 illustrates the partitioned zones and corresponding grain size distributions at the interface. Particularly, Fig. 10(a) shows the SEM image of bonding interface in Fig. 9(c), which is subdivided into three distinct regions: 414N-NI adjacent to the 414N side, interface, and 42CrMo-NI adjacent to the 42CrMo side. The grain size distributions across these zones are quantified. 414N cladding interior in Fig. 9(b) is characterized by an average grain size of 8.8 μm with a broad distribution range of ≤30 μm, as shown in Fig. 10(b). 414N-NI region in Fig. 9(c) exhibits refined grains with an average size of 4.1 μm and a size distribution range of ≤15 μm, as shown in Fig. 10(c). The interface region in Fig. 9(c) demonstrates further grain refinement to 4.0 μm with a size distribution range of ≤12 μm, as shown in Fig. 10(d), indicating enhanced grain size control due to the synergistic interaction between 414N and 42CrMo. This refinement mechanism contributes to improved interfacial bonding strength and mechanical performance. As for the 42CrMo-NI region in Fig. 9(c), the grain size increases to 8.6 μm with a size distribution range of ≤16 μm, as shown in Fig. 10(e). For the 42CrMo-FI region in Fig. 9(d), the grain size further decreases to 6.8 μm with a size distribution range of ≤16 μm.

Figure 11 presents the distribution of geometrically necessary dislocations (GND) density values, while Fig. 12 illustrates the proportional evolution of LAGBs and HAGBs. The spatial variation in GND density values reflects gradients in plastic deformation intensity. As shown in Fig. 11(b), the 414N cladding interior exhibits lower average GND density values compared to 414N-FI in Fig. 11(a), indicating that the cladding edge experiences more severe plastic deformation. A progressive decline in GND density magnitudes can be observed toward the cladding interior, suggesting a gradual attenuation of plastic deformation intensity. Analysis of grain

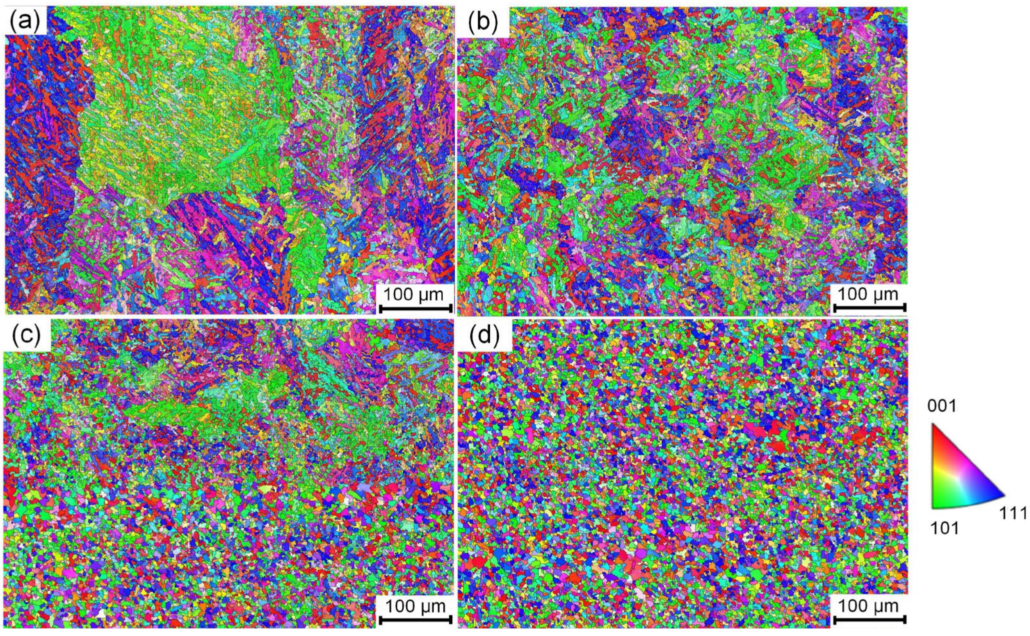

Fig. 7: Low-magnification EBSD-IPF maps: (a) 414N-FI; (b) 414N cladding interior; (c) bonding interface; (d) 42CrMo-FI

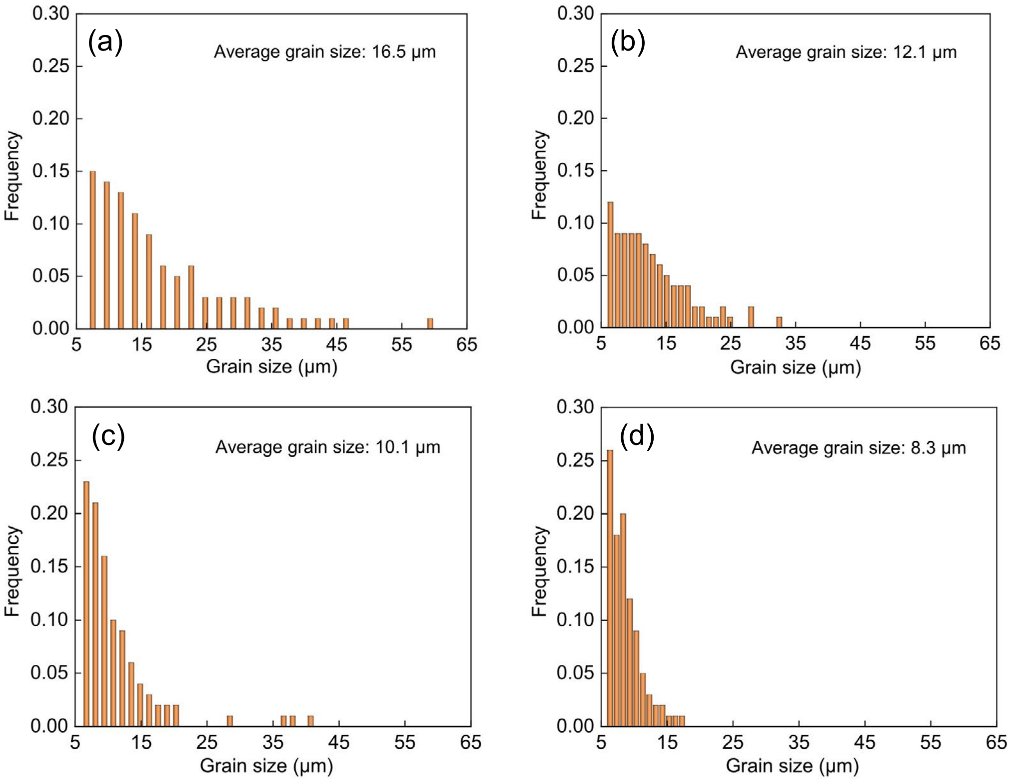

Fig. 8: Grain size distribution in low-magnification EBSD-IPF maps: (a) 414N-FI; (b) 414N cladding interior; (c) bonding interface; (d) 42CrMo-FI

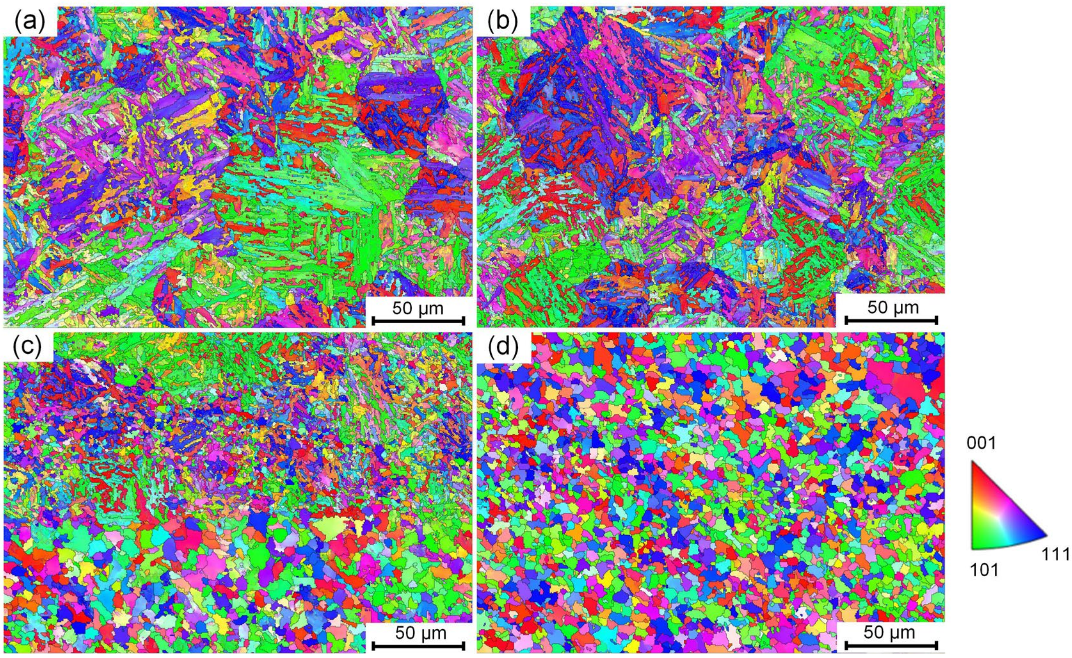

Fig. 9: High-magnification EBSD-IPF maps: (a) 414N-FI; (b) 414N cladding interior; (c) bonding interface; (d) 42CrMo-FI

boundary angle distributions in Fig. 12 reveals structural transitions across the cladding-to-substrate interface. At the 414N-FI region in Fig. 12(a), LAGBs dominate at 60.1%, with HAGBs accounting for 39.9%. Transitioning toward the 414N cladding interior in Fig. 12(b), the LAGBs decrease to 58.3%, while HAGBs increase to 41.7%. For the bonding interface shown in Fig. 12(c), the LAGBs decrease to 46.3%, while HAGBs increase to 53.7%, which reflects the position-dependent variation of LAGB and HAGB fractions. For the grain boundary angles, Figs. 12(a) and (b) exhibit bimodal distribution characteristics in LAGBs and HAGBs. Notably, for the substrate side in Fig. 12(d), the 42CrMo region displays a significantly lower LAGB proportion of 10.1% and a predominant HAGB fraction of 89.8%. This distinct boundary architecture in the substrate features lower internal stress concentration, thereby enhancing fatigue resistance under prolonged thermomechanical service conditions.

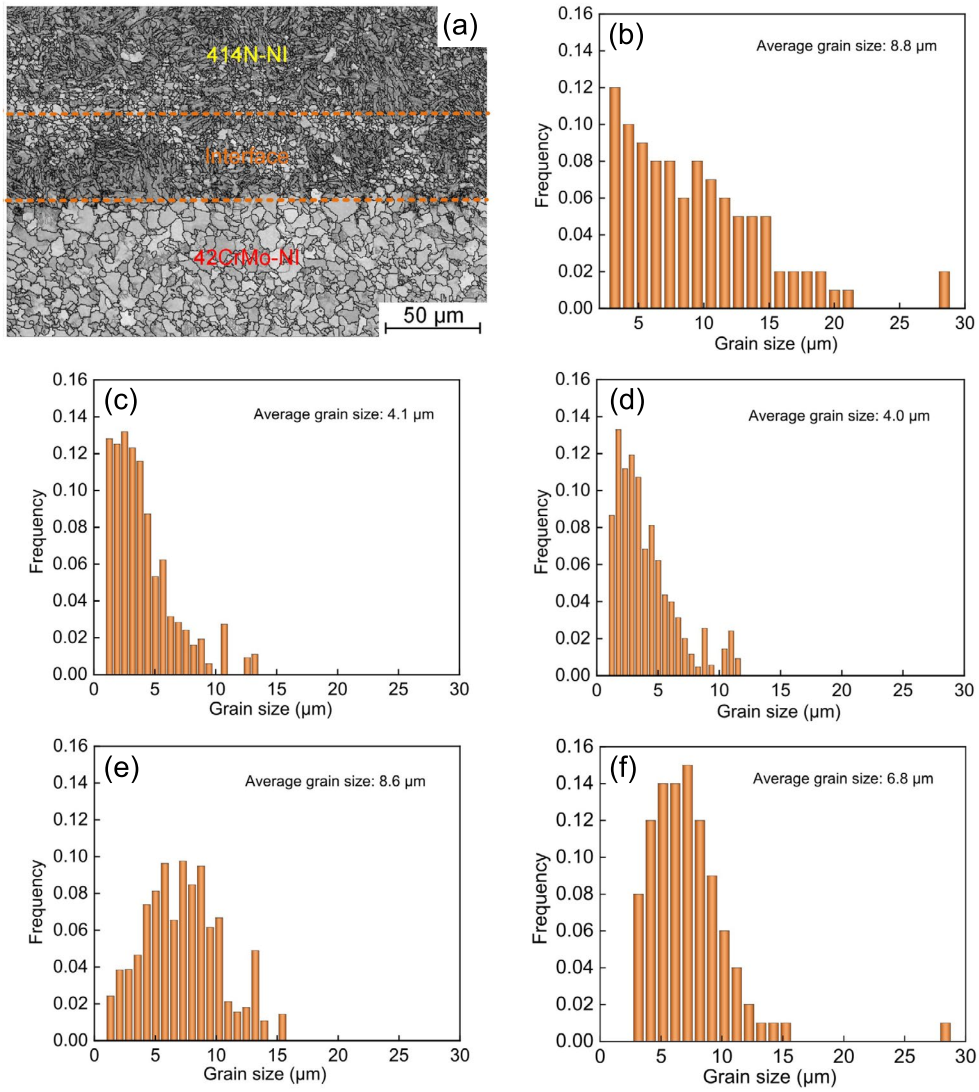

Fig. 10: High-magnification bonding interface microstructure and grain size distribution: (a) SEM of bonding interface in Fig. 9(c); (b) 414N cladding interior in Fig. 10(a); (c) 414N-NI in Fig. 10(a); (d) interface in Fig. 10(a); (e) 42CrMo-NI in Fig. 9(c); (f) 42CrMo-FI in Fig. 9(d)

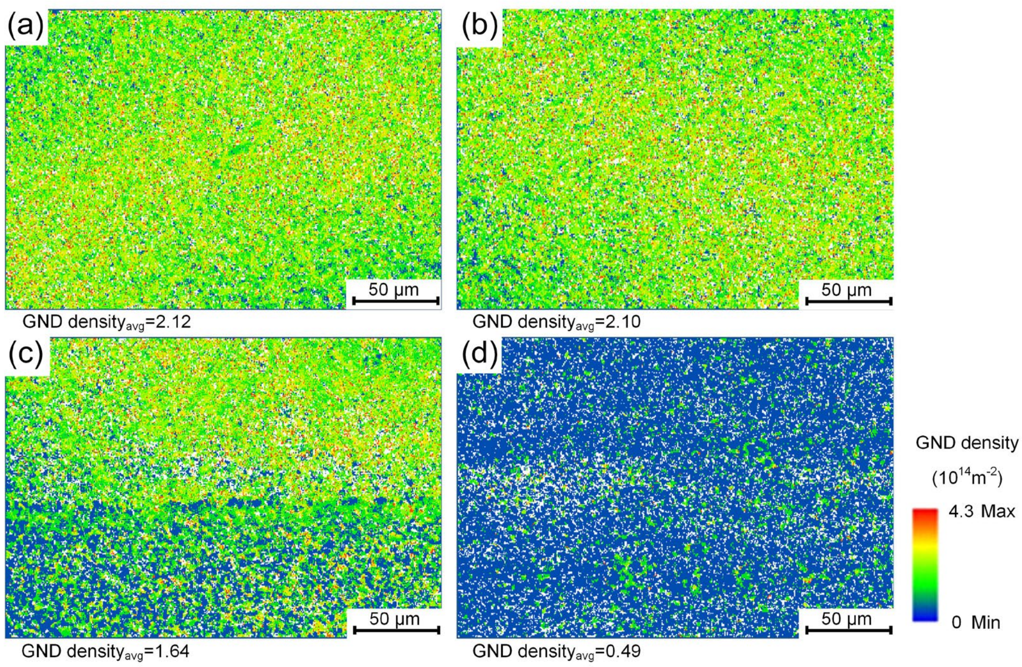

Fig. 11: GND density maps of different regions: (a) 414N-FI; (b) 414N cladding interior; (c) bonding interface; (d) 42CrMo

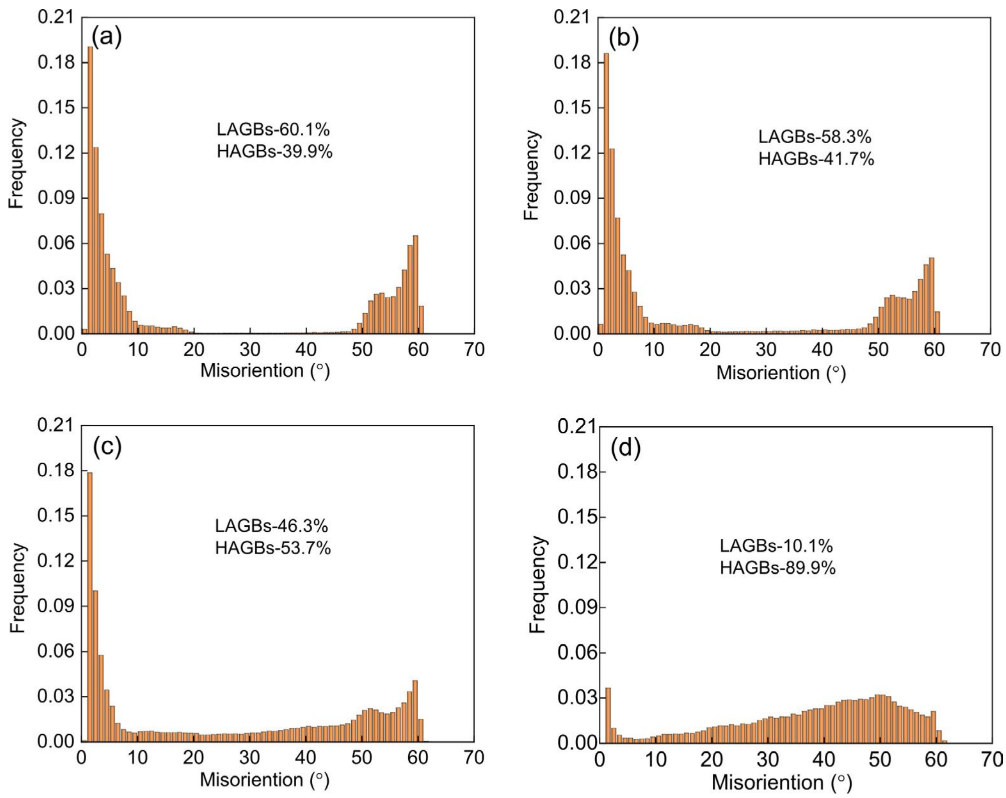

Fig. 12: Proportion map of low-angle and high-angle grain boundaries: (a) 414N-FI; (b) 414N cladding interior; (c) bonding interface; (d) 42CrMo

Owing to prolonged service under cyclic thermomechanical loading conditions involving elevated temperatures and pressures, the surface plastic deformation of the continuous casting composite roller is caused by the contact stress. To quantitatively characterize the orientation distribution of grains, pole figure analysis was systematically conducted from the 414N-FI to 42CrMo, as illustrated in Fig. 13. From the 414N-FI side in Figs. 13(a1–a3) to the 42CrMo substrate side in Figs. 13(d1–d3), discrete texture distributions are attributed to the absence of pronounced crystallographic orientation development under multidirectional cyclic stresses. Quantitative texture analysis reveals significant spatial variations. The cladding periphery in Figs. 13(a1–a3) demonstrates a maximum basal texture intensity of 4.6. The 414N cladding interior in Figs. 13(b1–b3) shows reduced texture intensity to 2.39, and 42CrMo regions in Figs. 13(d1–d3) maintain minimal texture development. This texture gradient directly correlates with deformation heterogeneity. Enhanced texture intensity at 414N-FI originates from accumulated plastic strain during prolonged service, whereas diminished texture strength in interior/substrate regions reflects limited deformation penetration. Such microstructural evolution suggests that strain localization preferentially occurs at surface layers under cyclic loading, while the 42CrMo side retains near-original texture characteristics.

Figure 14 presents recrystallization distribution maps of the bonding under low- and high-magnification fields, employing a crystallographic classification system based on grain orientation gradients[37], where microstructural constituents are categorized as follows: recrystallized grains (blue, orientation gradients < 2°), substructured grains (yellow, 2°–7°), and deformed grains (red, >7°). Owing to prolonged thermomechanical service under elevated temperatures and pressures, the 414N microstructure predominantly consists of deformed grains, as evidenced in Figs. 14(a1, a2) and (b1, b2). It can be inferred that the 414N after online service is dominated by deformed grains, which store a high level of plastic strain energy, with the recrystallized grains proportion remaining at around 20%. At the bonding interface, the introduction of the substrate side significantly increases the proportions of recrystallized and recovered structures. Under high magnification, remarkably substructured grains are observed in the 42CrMo substrate near the interface, which differ from the change of the recrystallized grains and deformed grains that show a monotonic increase or decrease from the 414N side to the 42CrMo side. This phenomenon can be explained by the change in stress distribution in the substrate side region of the bonding interface.

The surface of the composite roller experiences complex stress environments involving high temperatures and high pressures during service, resulting in substantial storage of plastic strain energy within the material, primarily manifested as deformed grains. The 42CrMo side with low strength facilitates dispersion and alleviation of stresses, thereby reducing constraints on originally high-stress grains and creating more favorable conditions for recrystallized grains. Furthermore, structural differences between the matrix material and coating material at the bonding interface promote grain refinement in this transitional zone. The increased grain boundary energy associated with fine-grained structures promotes recovery processes through grain boundary migration and rearrangement, thereby leading to a higher density of recovered microstructures in the interface-adjacent regions of the 42CrMo steel matrix.

During material processing, heat transfer occurs through thermal conduction and radiation mechanisms to both the cladding layer and substrate of the rollers, imposing significant thermal input. This periodic thermal input results in repetitive heating-cooling cycles experienced by the rollers, a phenomenon termed thermal cycling[38]. This thermal cycling phenomenon exerts significant impacts on the microstructures, mechanical properties, and residual stresses of the continuous casting process. As shown in Fig. 15, the histogram of recrystallization build-up in different regions of the continuous casting process follows the zoning methodology detailed in Fig. 10(a). The cladding and interface regions are predominantly composed of deformed grains, with the proportion of recrystallized grains demonstrating a progressive increase as the distance from the cladding periphery increases. Notably, the substructured grain fraction exhibits relatively elevated proportions in the 42CrMo-NI, which may be attributable to crystallographic growth driven by thermal flux propagation and localized thermomechanical stresses. The interplay between thermal gradients and stress fields induces preferential substructured grain formation in the 42CrMo-Ni region.

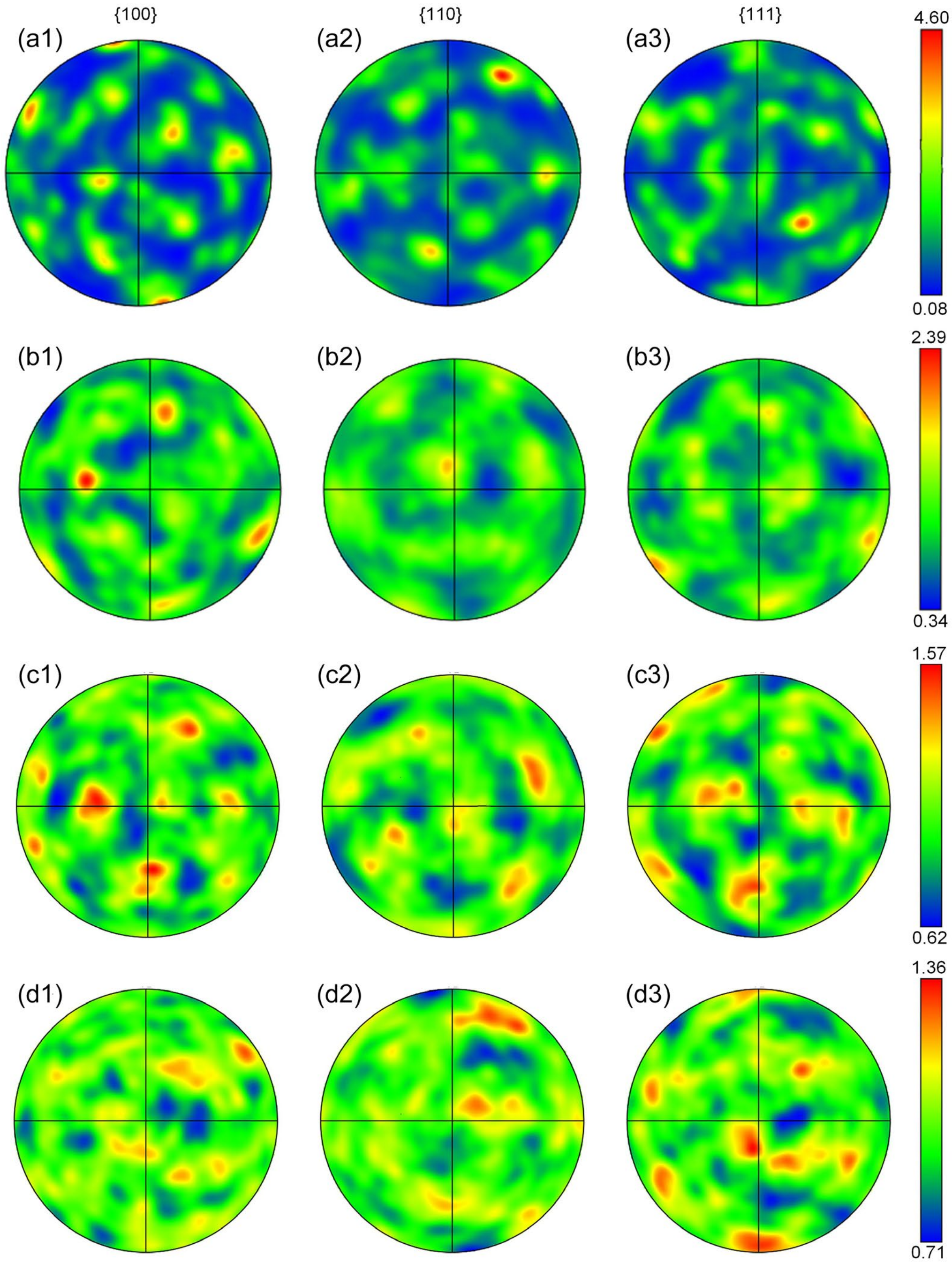

Fig. 13: {100} {110} {111} polar plots of different zones from the cladding to the substrate: (a1–a3) 414N-FI; (b1–b3) 414N cladding interior; (c1–c3) bonding interface; (d1–d3) 42CrMo

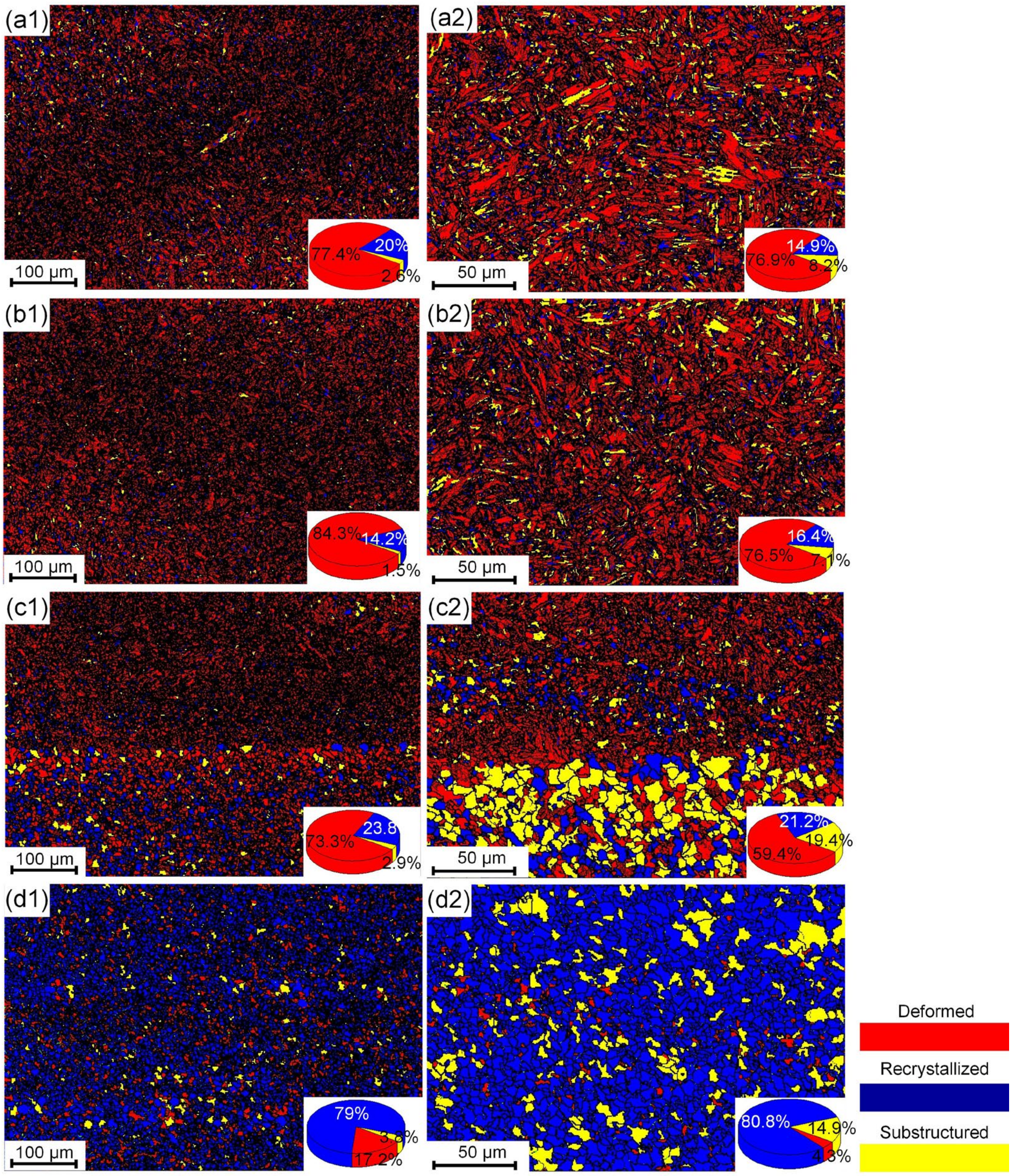

Fig. 14: Recrystallization distribution in low and high magnification field of view: (a1, a2) 414N-FI; (b1, b2) 414N cladding interior; (c1, c2) bonding interface; (d1, d2) 42CrMo

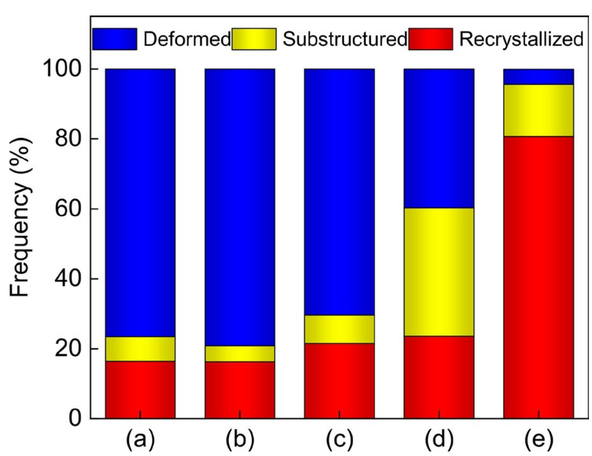

Fig. 15: Histogram of recrystallization build-up in different regions: (a) 414N cladding interior; (b) 414N-NI; (c) interface; (d) 42CrMo-NI; (e) 42CrMo-FI

3.4 Micropores after online service

Through three-dimensional reconstruction and defect characterization by integrating extensive 2D cross-sectional imaging data, a high-fidelity 3D reconstructed model was computationally reconstructed, establishing the foundational framework for spatial visualization. Based on high-resolution 3D visualization models generated through X-ray computed tomography, distinct structural features under varying stress states can be precisely identified, including quantitative variations in pore population, morphological complexity, dimensional spectrum, spatial configuration patterns, and dynamic evolutionary pathways. To systematically quantify defect morphology, the sphericity parameter ψ was employed as a pivotal shape descriptor for distinguishing between near-spherical geometries and irregular configurations. This metric establishes a correlation between three-dimensional form characteristics and two-dimensional surface area measurements[39], mathematically expressed as:

$$\psi = \frac{\pi}{6A}(6A)^{2/3} \quad (1)$$

where V represents the volume of the defect, and A represents the surface area.

As illustrated in Fig. 16, comparative X-ray computed tomography analyses between the 414N cladding side and bonding interface reveal distinct defect distribution patterns. Quantitative characterization in Fig. 17, through a statistical evaluation of micropore population and sphericity across specimen subregions, confirms defect accumulation within the 414N-NI interfacial zone. The volume ratio of defects in the 414N-FI region demonstrates a 16.4-fold escalation from 0.0019% to 0.0312%, paralleled by an exponential surge in defect count from 59 to 396. Concurrently, the ψ_{min} at the bonding interface reduces to 0.59. Multiparametric statistical analysis of equivalent diameter, volumetric distribution, and sphericity, quantified through histogram distributions and Gaussian fitting curves, indicates that 414N-FI defects equivalent diameter <25 μm and randomly dispersed. In contrast, the bonding interface defects are characterized by

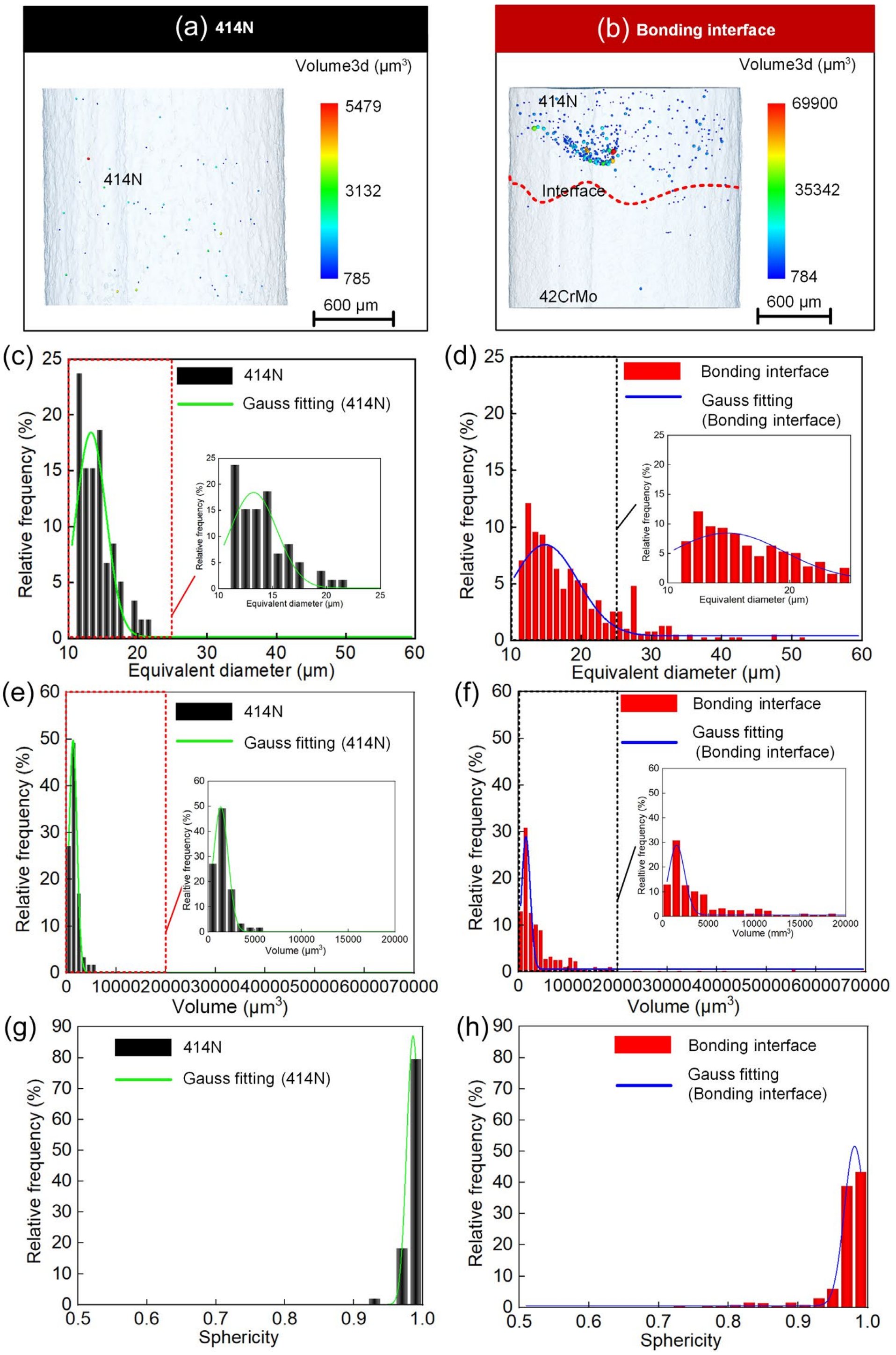

Fig. 16: 3D geometric reconstruction and data statistics: (a) 414N cladding; (b) bonding interface; (c) and (d) equivalent diameter of micropores; (e) and (f) volume of micropores; (g) and (h) sphericity of micropores

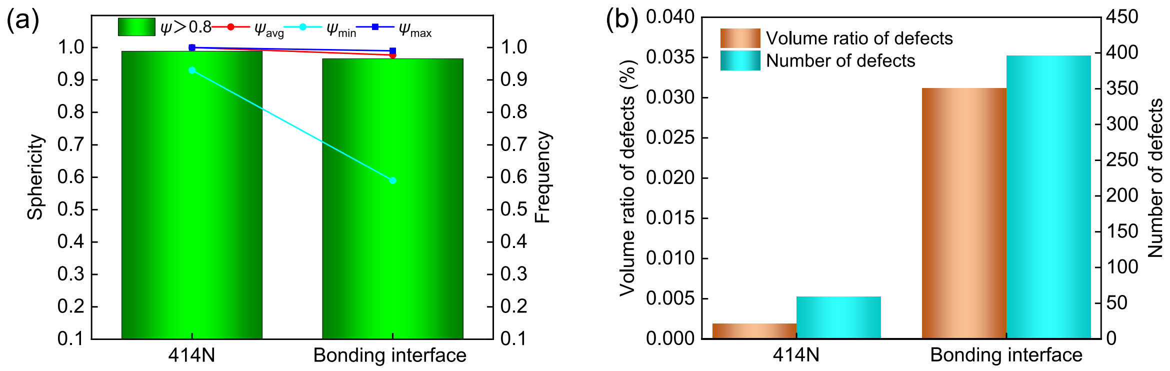

Fig. 17: Statistics of micropores in different regions: (a) sphericity data statistics; (b) number of defects and volume ratio of defeces

a pronounced defect cluster and irregular large-scale defects (equivalent diameter >50 μm). These geometrically complex defects easily cause stress concentration and potential microcrack initiation, thus severely threatening the service integrity via accelerated fatigue-failure mechanisms[40,41]. Therefore, to address interfacial cluster and irregular large-scale defects in decommissioned composite rollers, a surfacing remanufacturing strategy is proposed, including complete removal of defect-enriched layers, followed by gradient additive surfacing applied onto this newly created substrate to restore the dimensions, and final precision machining to standard dimensions.

4 Conclusions

(1) The composite roller exhibits a periodic undulating interface with alternating peak-valley features and typical gradient evolution characteristics. The interfacial element diffusion layer thickness forms a gradient distribution of 38–55 μm at the peaks and valleys, caused by the temperature gradient fluctuations within the molten pool. EDS-map scanning and EDS-line scanning results reveal continuous concentration gradients of alloy elements (Fe, Cr, Mn) across the interface, with significant interdiffusion occurring in both peak and valley regions, which contributes to the interfacial metallurgical bonding.

(2) The 414N cladding-42CrMo substrate system reveals a pronounced gradient in grain structure and boundary characteristics. The 414N cladding boundary transitions to the 42CrMo substrate with grain refinement to 4 μm at the interface under high-magnification observation, followed by coarsening to 6.8 μm in the 42CrMo substrate zone. GND density analysis confirms that this rigid-flexible gradient structure effectively mitigates local strain energy density and alleviates stress concentration under thermomechanical loading, highlighting the critical role in enhancing bonding interface compatibility and mechanical reliability.

(3) X-ray computed tomography reveals defect aggregation at the bonding interface of post-service composite rollers. The volume ratio of defects exhibits a 16.4-fold increase from 0.0019% (414N) to 0.0312% (bonding interface), accompanied by exponential growth in defect count (59 to 396). Compared to randomly dispersed 414N cladding defects smaller than 25 μm, bonding interfacial defects display reduced sphericity (ψ_{min}=0.59) and clustered morphologies with equivalent diameters exceeding 50 μm.

(4) Irregular large-area defects concentrated at the bonding interface may produce localized stress concentration and are prone to form microcracks under thermo-mechanical cycling during the next online service. To address interfacial microvoid defects in decommissioned composite rollers, a gradient machining-gradient surfacing remanufacturing strategy was established, including complete removal of defect-enriched layers, followed by gradient surfacing implementation starting from the original substrate interface position, and final precision machining to standard dimensions. This approach achieves full restoration of service performance by reconstructing spatial gradient characteristics of bonding interfaces.

Acknowledgments

This work was supported by the National Natural Science Foundation of China (Nos. 52205406, 52375390) and the Natural Science Foundation project of Hebei Province (Nos. E2024203066, BJ2025139, E2023203260).

Conflict of interest

The authors declare that they have no conflict of interest.

References

[1] Zhang J S, Xiao G Q, Peng J, et al. Gradient structure design and welding-hammering hybrid remanufacturing process of continuous casting rollers. Materials, 2022, 15(23): 8588.

[2] Marushchak O P, Bishchak T R, Baran Y D, et al. Unit for physical modeling of the operation of a continuous-caster roller under thermal-fatigue conditious. Metallurgist, 2012, 55(9–10): 664–667.

[3] Yong Z Z, Li J, Qing Y Z, et al. Application of remanufacturing technology in imported roll EDT machine. Applied Mechanics and Materials, 2014, 705: 243–246.

[4] Liang X, Zhang X, Wang W, et al. Revealing the crack formation mechanism of SS/NiTi heterogeneous materials fabricated by wire arc additive manufacturing. Materials Characterization, 2025, 223: 114879.

[5] Peng Y W, Hao Y, Chang J C, et al. Compression behavior of 316L lattice structures produced by indirect additive manufacturing. China Foundry, 2023, 20(2): 83–88.
[6] Ji C, Niu H, Li Z X, et al. Deformation law and bonding mechanism of 45 carbon steel/316L stainless steel cladding tubes fabricated by three-roll skew rolling bonding process. Journal of Materials Processing Technology, 2024, 325: 118277.
[7] Nayir S, Knapp L G, Plotkowski A, et al. Localized orientation gradients in additively manufactured stainless steel 316H structure. Materials Characterization, 2025, 223: 114860.
[8] Yi X, Bai X W, Yu R Y, et al. Microstructure and mechanical properties of laminated Ti-TiBw/Ti composites fabricated by wire arc additive manufacturing. Materials Characterization, 2024, 218: 114512.
[9] Viňáš J, Brezinová J, Guzanová A, et al. Evaluation of the quality of cladding deposited on continuous steel casting rolls. International Journal of Materials Research, 2013, 104(2): 183–191.
[10] Viňáš J, Brezinová J, Guzanová A. Analysis of the quality renovated continuous steel casting roller. Sadhana, 2013, 38(3): 477–490.
[11] Lei Z, Su W. Research and application of a rolling gap prediction model in continuous casting. Metals, 2019, 9(3): 380.
[12] Wang S Q, Chen K M, Cui X H, et al. Effect of alloying elements on thermal wear of cast hot-forging die steels. Journal of Iron and Steel Research International, 2006, 13(5): 53–59.
[13] Li J X, Ye Y M, Lu H Q, et al. Effects of laser power on friction-wear behaviors of NiCoCrAlY coatings at high temperature. Materials Research Express, 2019, 6(12): 1265.
[14] Wang T, Zhao W, Yun Y, et al. A dynamic composite rolling model based on Lemaitre damage theory. International Journal of Mechanical Sciences, 2024, 269: 109067.
[15] Dai S, Zhang H, Bian Z, et al. Insight into the recrystallization behavior and precipitation reaction of in-situ nano TiB_2/Al-Cu-Mg composite during heat treatment. Materials Characterization, 2021, 181: 111458.
[16] Li M F, Zhang H, Zeng Y M, et al. A perspective on investigating transition metal high-entropy alloys for high-temperature applications. Acta Materialia, 2022, 240: 118313.
[17] Chen H, Qin S, Men S, et al. Ni/Ti Amed part/substrate interface reconfiguration under electropulsing. Journal of Materials Research and Technology, 2024, 33: 5898–5908.
[18] Yan M, Li R, Bi X, et al. Microstructure and properties of extreme high-speed laser cladded nickel-based coatings assisted by ultrasonic impact treatment. Surface & Coatings Technology, 2025, 498: 131820.
[19] Liu D F, Li C, Xin S, et al. High-temperature friction and wear behaviors of the laser in-situ synthesized VB_2 reinforced NiCrBSi alloy-based composite coating. Optics and Laser Technology, 2025, 184: 112505.
[20] Higashino S, Miyashita D, Ishimoto T, et al. Low Young's modulus in laser powder bed fusion processed Ti-15Mo-5Zr-3Al alloys achieved by the control of crystallographic texture combined with the retention of low-stability bcc structure. Additive Manufacturing, 2025, 102: 104720.
[21] Yao W, Khan A M, Dai S, et al. Advancements in high-entropy alloys: Exploring mechanical and corrosion properties of gradient-cast lightweight MgAlCuZnGd multi-component alloys. Journal of Alloys and Compounds, 2025, 1018: 179112.
[22] Qiu J, Li Y D, Zhou H W, et al. Exploring the interfacial microstructure evolution and bonding properties of Al/steel composite plates fabricated through semi-solid cast-rolling. Metals, 2025, 15(2): 162.
[23] Chen H, Qin S, Kong X, et al. Brittle precipitates regulation in Ni/Ti composition gradient materials under pulsed current. Journal of Materials Research and Technology, 2025, 34(3): 211–237.
[24] Peng B, Jie J C, Sun J, et al. Synergistic deformation and fracture behavior of heterostructure Cu/1010 steel bimetal laminated composites. Materials Science & Engineering: A, 2023, 888: 145835.
[25] Jafari A, Bahreini S R, Yazdanian R. Empirical, analytical and numerical approaches to failure analysis of a frictional power transmission composite roller. Engineering Failure Analysis, 2015, 52: 61–74.
[26] Huang K, Han X. Laser cladding of a Ti-Zr-Mo-Ta-Nb-B composite coating on Ti60 alloy to improve wear resistance. Coatings, 2024, 14(10): 1247.
[27] Chen H, Zi X, Han Y, et al. Microstructure and mechanical properties of additive manufactured W-Ni-Fe-Co composite produced by selective laser melting. International Journal of Refractory Metals and Hard Materials, 2020, 86: 105111.
[28] Li M, Luo Z, Zhou H, et al. Interface microstructure and properties of 42CrMo/Cr5 vacuum billet forged composite roll. Materials, 2024, 18(1): 122.
[29] Hou Z W, Dong Y W, Jiang Z H, et al. Interface bonding mechanism and heat treatment of the composite roll manufactured by electroslag remelting cladding method. Journal of Materials Research and Technology, 2022, 19: 4115–4127.
[30] Liu J, Miao Y, Wang Z, et al. Improved interfacial strength in bimetallic additive manufacturing of aluminum bronze/steel by controlling interface melting. Journal of Manufacturing Processes, 2024, 121: 333–342.
[31] Chandrasekaran S, Hari S, Amirthalingam M. Functionally graded materials for marine risers by AM for high-temperature applications: Experimental investigations. Structures, 2022, 35: 931–938.
[32] Chen C Y, Xie Y C, Yi S, et al. Ductile and high strength Cu fabricated by solid-state cold spray additive manufacturing. Journal of Materials Science & Technology, 2023, 134: 234–243.
[33] Wei S Y, Wuu D, Soh V, et al. High throughput additive manufacturing and characterization of immiscible Cu-Fe binary system using compositional gradient approach. Journal of Alloys and Compounds, 2025, 1014: 178770.
[34] Amiri V, Moosavy N H. Microstructural study of additively-manufactured carbon steel-stainless steel 316L-Inconel 625 functionally graded material: Simulation and experimental approaches. Journal of Materials Research and Technology, 2024, 311: 164–1170.
[35] Cheng G, Yin N, Zheng Q, et al. Numerical simulation of surface thermal analysis and cooling optimization of continuous casting rolls. Crystals, 2024, 15(1): 41.
[36] Zhang Y, Li Z, Tang Y, et al. Research on heat transfer behavior and deformation characteristics of casting rollers in twin-roll casting process. International Journal of Thermal Sciences, 2025, 214: 109843.
[37] Liang T, Xing S H, Liu G J, et al. Numerical simulation of hardfacing remanufacturing for large-scale damaged grinding roller. The International Journal of Advanced Manufacturing Technology, 2021, 118(7–8): 2613–2649.
[38] Han J, Li X, An T, et al. Failure analysis and simulation of IGBT under active and passive thermal cycling. Microelectronics Reliability, 2025, 167: 115638.
[39] Gao C, Li L, Chen X, et al. The effect of surface preparation on the bond strength of Al-St strips in CRB process. Materials & Design, 2016, 107: 205–211.
[40] Zhang Z, Gao Z, Tu H, et al. Three-dimensional characteristics and evolution of creep cavity and microcrack of HR3C austenitic heat resistant steel after long-term creep at 650 °C. Engineering Failure Analysis, 2024, 164: 108634.
[41] Sharmini A, Zenn H Y, Anita S B, et al. Micro-computed tomography evaluation of dentinal microcracks following canal preparation with thermomechanically heat-treated engine-driven files. Australian Endodontic Journal, 2021, 47(3): 520–530.